



Mn_{0.2}Cd_{0.8}S nanowires modified by CoP₃ nanoparticles for highly efficient photocatalytic H₂ evolution under visible light irradiation

Qun-Zeng Huang^a, Ze-Juan Tao^a, Li-Qun Ye^a, Hong-Chang Yao^{b,*}, Zhong-Jun Li^{b,*}

^a College of Chemistry and Pharmaceutical Engineering, Engineering Technology Research Center of Henan Province for Solar Catalysis, Nanyang Normal University, Nanyang 473061, PR China

^b College of Chemistry and Molecular Engineering, Zhengzhou University, Zhengzhou 450001, PR China



ARTICLE INFO

Keywords:

Photocatalytic H₂ evolution

Mn_xCd_{1-x}S

Cobalt phosphide

Co-catalyst

Heterojunction

ABSTRACT

Development of highly efficient and low-cost noble metal-free co-catalysts for photocatalytic H₂ evolution from water splitting has been aiming at a long-term goal of a renewable hydrogen economy. Herein, a series of novel Mn_{0.2}Cd_{0.8}S/CoP₃ composites have been successfully prepared through loading CoP₃ nanoparticles on the surface of one dimensional (1D) Mn_{0.2}Cd_{0.8}S nanowires (NWs) by a facile solvothermal method. Under visible light ($\lambda \geq 420$ nm) irradiation, the as-prepared Mn_{0.2}Cd_{0.8}S/CoP₃ composite with 2.87 wt% of CoP₃ displayed the highest photocatalytic H₂ evolution activity with a corresponding H₂ evolution rate of 29.53 mmol g⁻¹ h⁻¹ and an apparent quantum yield of 29.2% at 420 nm, which was about 5.02 times higher than that of pure Mn_{0.2}Cd_{0.8}S and 1.79 times than that of Mn_{0.2}Cd_{0.8}S/Pt-1.5 wt%. Moreover, the Mn_{0.2}Cd_{0.8}S/CoP₃ composite exhibited excellent photostability. The superior photocatalytic activity of Mn_{0.2}Cd_{0.8}S/CoP₃ composite was predominantly attributed to the synergistic effects of highly efficient charge separation efficiency and sufficient active sites for H₂ evolution reaction. This work revealed that low-cost CoP₃ can replace noble metal Pt as a highly efficient co-catalyst for enhancing the photocatalytic activity of semiconductor materials.

1. Introduction

The conversion of solar energy to hydrogen energy by photocatalytic H₂ evolution from water splitting represents a promising strategy for addressing both the energy crisis and environmental problems [1–4]. One of the key challenges for the application of photocatalytic H₂ evolution is the development of efficient photocatalysts. Despite the fact that tremendous semiconductor materials have been explored for photocatalytic H₂ evolution since the pioneering discovery of photocatalytic water splitting in 1972 [5], developing of novel visible light-responsive photocatalysts with sufficient charge separation ability, high photocatalytic activity and stability to cater for the demand of practical applications, is still a challenging task.

Over the past few years, Mn_xCd_{1-x}S solid solution, as a member of ternary chalcogenides, has attracted increasing attention in the field of photocatalytic H₂ evolution due to its tunable electronic structure, excellent visible-light absorption capacity and enhanced photocatalytic performance [6,7]. However, pure Mn_xCd_{1-x}S solid solution still suffers from fast recombination of photogenerated charge carriers and severe photocorrosion. To address these issues, several effective strategies, involving morphological tailoring [8], metal doping [9,10],

constructing heterojunction [11,12] and co-catalyst modification [13–16], have been employed to further upgrade the photocatalytic efficiency of Mn_xCd_{1-x}S. Among these strategies, controlling the sizes and morphology of Mn_xCd_{1-x}S is crucial to improving its photocatalytic activity. For example, Liu's et al. [8] synthesized the flower-like Mn_{0.8}Cd_{0.2}S microspheres and found that the microspheres exhibited better photocatalytic H₂ evolution activity than Mn_{0.8}Cd_{0.2}S nanoparticles. To date, most morphologies of the Mn_xCd_{1-x}S solid solutions reported are irregular particles and microspheres. However, there are few reports about the preparation and photocatalytic activity of 1D Mn_xCd_{1-x}S solid solutions. In fact, 1D nanostructures is not only favorable for the separation of electron–hole pairs as they can shorten the diffusion pathway of charge carriers, but also useful to enhance the light absorption properties due to their high length-to-diameter ratios [17–20]. Besides, co-catalyst modification also exhibits great potential in enhancing photocatalytic H₂ evolution activity due to the fact that it not only can effectively promote the separation of photogenerated charge carriers, but also afford the low activation potentials as well as abundant active sites [21–23]. Nevertheless, to date, the most efficient co-catalysts remain dominated by noble metals, particularly Pt, which suffer from high cost, in terms of large-scale application. Hence,

* Corresponding authors.

E-mail addresses: yaohongchang@zzu.edu.cn (H.-C. Yao), lizhongjun0713@163.com (Z.-J. Li).

exploring the highly efficient and noble metal-free co-catalysts for enhancing the photocatalytic H₂ evolution activity of Mn_xCd_{1-x}S solid solution, is a topic of current interest.

Recently, transition metal phosphides, such as Ni₂P [24–26], Fe₂P [27,28], MoP [29,30], Zn₃P₂ [31], WP [32], etc. have been widely explored as promising co-catalysts in the field of photocatalytic H₂ evolution due to their outstanding efficiency, good stability and low cost. Since Fu's et al. [33] first found that Co₂P could be used as an efficient co-catalyst for enhancing the photocatalytic H₂ evolution activity of CdS nanorods, cobalt phosphide has attracted much attention in promoting the photocatalytic H₂ evolution activity of some photocatalysts [34], including CdS [35–40], TiO₂ [41], g-C₃N₄ [42,43], Cd_xZn_{1-x}Se [44] and Cd_xZn_{1-x}S [45]. For example, Du et al. [36] found that the highest H₂ evolution rate of ~500 μmol mg⁻¹ h⁻¹ and the apparent quantum yield of ~35% could be realized by loading amorphous CoP_x on the surface of CdS nanorod under visible light irradiation. CoP/Cd_{0.5}Zn_{0.5}S hybrids were prepared by Ge's et al. [45] and displayed the highest H₂ evolution rate of 734 μmol h⁻¹, which was about 20 times higher than that of pure Cd_{0.5}Zn_{0.5}S and even 2 times than that of Pt/Cd_{0.5}Zn_{0.5}S. These results mentioned above implied that cobalt phosphides could be potentially serve as promising noble metal-free co-catalysts. Therefore, it is expected that the synergistic effect of constructing 1D nanostructures and loading cobalt phosphide co-catalyst will further promote charge carriers separation of Mn_xCd_{1-x}S solid solution and endow it with more active sites for H₂ evolution. To the best of our knowledge, there is no report on the application of 1D Mn_xCd_{1-x}S with cobalt phosphide as a co-catalyst for photocatalytic H₂ evolution.

On the basis of this background, 1D Mn_xCd_{1-x}S (0.1 ≤ x ≤ 0.3) solid solutions with nanowires morphology were firstly synthesized via a facile solvothermal strategy. Among them, Mn_{0.2}Cd_{0.8}S NWs demonstrated the best photocatalytic performance (as discussed later). Thus, Mn_{0.2}Cd_{0.8}S was used in the following study. Herein, for the first time, we have engaged in a study of the synthesis of Mn_{0.2}Cd_{0.8}S NWs decorated with CoP₃ nanoparticles by a solvothermal method, and investigated their photocatalytic properties towards H₂ evolution under visible light irradiation ($\lambda \geq 420$ nm). The present work provided the remarkable and novel observation that CoP₃ was used as co-catalyst for optimization of the photocatalytic H₂ evolution activity of Mn_{0.2}Cd_{0.8}S. Detailed characterizations of the structure, composition, BET surface areas and optical properties of the Mn_{0.2}Cd_{0.8}S/CoP₃ composite were performed. In addition, a possible photocatalytic mechanism of Mn_{0.2}Cd_{0.8}S/CoP₃ composite was also proposed based on the results of photoluminescence spectroscopy and photoelectrochemical measurements.

2. Experimental section

2.1. Materials

Manganese acetate tetrahydrate (Mn(CH₃COO)₂·4H₂O), cadmium acetate dihydrate (Cd(CH₃COO)₂·2H₂O), cobaltous nitrate hexahydrate (Co(NO₃)₂·6H₂O), thioacetamide (CH₃CSNH₂), ethylenediamine (C₂H₄(NH₂)₂), sodium sulfide nonahydrate (Na₂S·9H₂O), sodium sulfite (Na₂SO₃) and chloroplatinic acid (H₂PtCl₆·6H₂O, 37.5% Pt basis) were obtained from Aladdin Reagent Co., Ltd. All reagents used are of analytical grade and were used without further purification.

2.2. Synthesis of Mn_xCd_{1-x}S (0 ≤ x ≤ 1) samples

The Mn_xCd_{1-x}S (0 ≤ x ≤ 1) samples were prepared by using a simple solvothermal method. In a typical process, 9x mmol of Mn(CH₃COO)₂·4H₂O, 9(1-x) mmol of Cd(CH₃COO)₂·2H₂O and excessive amounts of thioacetamide were dissolved in 60 mL ethylenediamine. After stirring for 30 min, the mixture was transferred into a Teflon-lined (100 mL capacity) stainless steel autoclave and heated at 160 °C for

24 h. The system was cooled to room temperature, and the precipitates were collected by centrifugation, washed using distilled water and ethanol. The final products were obtained after drying in a vacuum oven at 60 °C for 12 h. The actual atomic ratio of Mn²⁺/Cd²⁺ in the as-prepared Mn_xCd_{1-x}S (0 ≤ x ≤ 0.3) samples was measured by inductively coupled plasma atomic emission spectroscopy (ICP-AES) and the analytical results were given in Table S1. The obtained ICP-AES result was almost consistent with the nominal values. For the sake of convenience, the as-prepared Mn_xCd_{1-x}S (0 ≤ x ≤ 0.3) samples were addressed with their nominal value.

2.3. Synthesis of Mn_{0.2}Cd_{0.8}S/CoP₃ composites

The Mn_{0.2}Cd_{0.8}S/CoP₃ composites were prepared by a facile solvothermal method. Briefly, 3 mmol of Mn_{0.2}Cd_{0.8}S powders were first dispersed in 60 mL of ethylenediamine, and then were sonicated for 30 min with 400 W of ultrasonic output power. Subsequently, the desired amount (7.3, 14.6, 21.9, 29.1, 36.4, 43.7 or 51.0 mg) of Co(NO₃)₂·6H₂O and five-fold yellow phosphorus were added to the Mn_{0.2}Cd_{0.8}S suspension with magnetic stirring for 30 min. Then the resultant suspension was transferred into a Teflon-lined (100 mL capacity) stainless steel autoclave, sealed and maintained at 140 °C for 12 h. After cooling down to room temperature, the precipitate was collected by centrifugation, washed with benzol, deionized water and ethanol three times each, and then dried in a vacuum oven at 60 °C for 24 h. According to the ICP-AES results, the actual loading content of CoP₃ was determined to be 0.73, 1.42, 2.15, 2.87, 3.58, 4.34 and 5.01 wt%, respectively. For comparison, pure CoP₃ was also synthesized by a similar solvothermal method in the absence of Mn_{0.2}Cd_{0.8}S.

2.4. Characterization

Elemental measurements of Mn, Cd and Co were determined by ICP-AES analysis using an Leeman Labs PROFILE SPEC spectrometer. Powder X-ray diffraction (XRD) patterns were recorded on a PANalytical X'PERT PRO diffractometer using Cu Kα radiation source ($\lambda = 1.54056$) with applied voltage and current of 45 kV and 40 mA respectively. Transmission electron microscopy (TEM), high-resolution transmission electron microscopy (HRTEM) images and STEM-EDX mapping were recorded by a JEOL JEM-2100 F transmission electron microscope. X-ray photoelectron spectroscopy (XPS) and VB-XPS spectra were collected with a monochromatic Al K αX-ray source on an ESCALAB250 mul-titechnique X-ray photoelectron spectrometer. UV-Vis diffuse reflectance spectra (UV-vis DRS) were performed by a Hitachi UH4150 UV-vis/NIR spectrophotometer. N₂ adsorption-desorption isotherms, pore-size distributions and Brunauer–Emmett–Teller (BET) surface area were obtained on a Micromeritics Tri-Star II 3020 surface area analyzer at 77.35 K. Photoluminescence (PL) spectra and time resolved photoluminescence (TRPL) spectra of the solid samples were recorded on an Edinburgh FLS980 fluorescence spectrophotometer.

Electrochemical and photoelectrochemical measurements were performed on an electrochemical analyzer (CHI660E) in a three-electrode system with the working electrodes of as-prepared photocatalyst films on fluorine-doped tin oxide (FTO), the reference electrode of Ag/AgCl, and the counter electrode of Pt foil. Na₂SO₄ (0.5 mol L⁻¹) aqueous solution was used as an electrolyte. The photocurrent measurements were taken at an applied potential of 0.6 V vs Ag/AgCl under visible light irradiation provided by a 300 W Xe lamp with a UV-cut off filter ($\lambda \geq 420$ nm) in 0.5 mol L⁻¹ of Na₂SO₄ aqueous solution. The electrochemical impedance spectroscopy (EIS) was carried out in the frequency range from 0.1 to 100,000 Hz with an AC voltage amplitude of 5 mV.

2.5. Photocatalytic activity test

The photocatalytic H₂ evolution activity of as-synthesized samples were carried out in an online CEL-SPH2N photocatalysis reaction system (CEAULIGHT, Science and Technology Ltd, Beijing, China) with a 500 mL quartz photoreactor connected to a closed gas circulation and evacuation system. Typically, 50 mg of the samples were dispersed in 100 mL of water containing Na₂S (0.5 mol L⁻¹) and Na₂SO₃ (0.5 mol L⁻¹). Prior to irradiation, the reactant solution was thoroughly degassed under flowing high-purity N₂ for 15 min to remove any dissolved O₂. The photocatalytic H₂ evolution reactions were performed with a 300 W Xe lamp as the source of visible light which was equipped with 420 nm cut-off filter. The evolved H₂ was analyzed automatically every 1 h through a gas chromatograph (GC-7920) equipped with a thermal conductivity detector with high-purity N₂ as a carrier gas.

The apparent quantum efficiency (AQE) for H₂ evolution was measured under the same photocatalytic reaction conditions except that a 420 nm band-pass filter was used instead of the UV cut-off filter. The number of incident photons was measured using a power meter (Thorlabs PM100D). The AQE was calculated according to the following equation:

$$\text{AQE} = \frac{2 \times \text{the number of evolved H}_2 \text{ molecules}}{\text{the number of incident photons}} \times 100\%$$

3. Results and discussion

3.1. XRD analysis

XRD analysis was characterized to investigate the phase purity and phase structure of the as-prepared samples and the results were displayed in Fig. 1. Fig. 1a exhibited the XRD patterns of the Mn_xCd_{1-x}S (0 ≤ x ≤ 0.3) samples together with the standard diffraction patterns of hexagonal CdS (JCPDS 65-3414) and hexagonal γ-MnS (JCPDS 40-1289). It could be seen that the diffraction peaks of the CdS (x = 0) samples were well indexed as hexagonal CdS. With increasing the x value in the Mn_xCd_{1-x}S (0 ≤ x ≤ 0.3) samples, the XRD peaks exhibited an obvious shift toward the higher angle, and the crystal phase of the Mn_xCd_{1-x}S samples gradually changed from hexagonal CdS to hexagonal γ-MnS, which implied that the Mn²⁺ incorporated into the lattice of the CdS and decreased the fringe lattice distance of the CdS due to the lower radius of Mn²⁺ (0.46 Å) than that of the Cd²⁺ ion (0.97 Å) [14]. Some of the similar phenomena have also been reported [7,11,46]. The successive shifts in the XRD patterns indicated that the Mn_xCd_{1-x}S (0.1 ≤ x ≤ 0.3) samples were not a mixture of CdS and MnS, but were attributable of solid solution. The lattice constants (a = b, c) of Mn_xCd_{1-x}S (0 ≤ x ≤ 0.3) samples were determined by the MDI Jade5.0 software. The obtained lattice parameters were listed in Table S2. The lattice parameter a and c for the as-prepared CdS unit cell was 4.13172 Å and 6.71008 Å, respectively, which was consistent with the standard data of CdS. Meanwhile, the lattice parameters a and c were found to decrease almost linearly with the increase of Mn mole fraction (Fig. S1). The result was in accord with Vegard's law [47–49], indicating a homogeneous solid solution structure of Mn_xCd_{1-x}S (0.1 ≤ x ≤ 0.3). Fig. 1b showed the XRD patterns of the Mn_xCd_{1-x}S (0.4 ≤ x ≤ 1) samples and the standard diffraction patterns of cubic a-MnS (JCPDS 06-0518). It was clearly seen that the diffraction peaks of MnS (x = 1) sample are consistent with the cubic a-MnS phase with rock salt type. With increasing the x value in the Mn_xCd_{1-x}S (0.4 ≤ x ≤ 1), some diffraction peaks of a-MnS appeared, indicating that the α-MnS impurities existed in the samples. This implied that γ-MnS was unstable and easily transformed into α phase MnS at high temperature or pressure [50,51]. The XRD pattern of the as-prepared CoP₃ sample was shown in Fig. 1c and all peaks could be indexed as a cubic CoP₃ (PDF No. 29-0496). The diffraction peaks at 16.21°, 23.11°, 28.33°, 32.91°, 36.83°, 40.56°, 53.10° and 58.64° belonged to the (110),

(200), (211), (220), (310), (222), (420) and (422) phase of a cubic CoP₃, respectively. No impurities such as Co(0) metal were detected, indicating that the products were rather pure. The representative XRD patterns of Mn_{0.2}Cd_{0.8}S/CoP₃ composites were showed in Fig. 1d. No obvious diffraction peaks of CoP₃ phase could be identified in all composite samples, indicating that the CoP₃ content was too low and insensitive for XRD characterization. The results suggested that the deposition of CoP₃ did not affect the crystalline structure of Mn_{0.2}Cd_{0.8}S solid solution. Nevertheless, the presence of CoP₃ in the composites can be easily proved by TEM and XPS techniques as will be discussed later.

3.2. TEM analysis

The morphology and microstructure of the samples were investigated by TEM and HRTEM. Fig. 2a showed the TEM image of Mn_{0.2}Cd_{0.8}S sample and the inset displayed the high-resolution image of the part marked by blue block diagrams. As shown in Fig. 2a, the Mn_{0.2}Cd_{0.8}S sample displayed 1D nanowires morphology and the Mn_{0.2}Cd_{0.8}S NWs have typically smooth surfaces throughout the entire wires with an average diameter of 40–65 nm and an average length of 0.5–3.0 μm. After loading CoP₃, no obvious difference could be identified between the shapes and surface nanostructures of Mn_{0.2}Cd_{0.8}S (Fig. 2b), which was accordance with the result of XRD analysis. The HRTEM image (Fig. 2c) showed that a large amount of CoP₃ nanoparticles were uniformly dispersed on the surface of Mn_{0.2}Cd_{0.8}S NWs, as marked by red block diagrams in Fig. 2c. More microstructural details of the interfacial region between Mn_{0.2}Cd_{0.8}S and CoP₃ in the Mn_{0.2}Cd_{0.8}S/CoP₃-2.87 wt% composite were observed in the HRTEM image displayed in Fig. 2d. The crystalline lattice spacing of 0.244 nm can be assigned to the (310) plane of cubic CoP₃ and the lattice spacing of 0.336 nm corresponds to the (002) plane of Mn_{0.2}Cd_{0.8}S. Furthermore, Fig. 3a-f displayed the STEM-EDX elemental mapping images of Mn_{0.2}Cd_{0.8}S/CoP₃-2.87 wt% composite. The result showed that all the major elements of Cd, Mn, S, Co and P were uniformly distributed in the structure of Mn_{0.2}Cd_{0.8}S/CoP₃-2.87 wt% sample, which further confirmed that CoP₃ nanoparticles were intimately deposited on the surface of Mn_{0.2}Cd_{0.8}S NWs. The TEM results indicated that intimate contact interfaces between Mn_{0.2}Cd_{0.8}S and CoP₃ were formed in the composite, which were beneficial for accelerating the separation of photo-generated charge carriers.

3.3. XPS analysis

XPS analysis was explored in order to gain deeper insight into the surface elemental composition and oxidation states of composite material. Fig. 4a presented the survey spectrum of the Mn_{0.2}Cd_{0.8}S/CoP₃-2.87 wt% sample, which proved the co-existence of Mn, Cd, S, Co and P elements as expected. In the Mn 2p XPS spectrum (Fig. 4b), the binding energies at 651.98 and 641.28 eV corresponded to 2p_{1/2} and 2p_{3/2} of Mn²⁺, respectively. As shown in Fig. 4c, Cd 3d spectrum displayed two peaks at 404.19 and 410.94 eV, corresponding to Cd 3d_{5/2} and Cd 3d_{3/2}, respectively, confirming the +2 oxidation state of Cd in Mn_{0.2}Cd_{0.8}S/CoP₃ composite. The XPS peaks located at 160.68 eV (S 2p_{3/2}) and 161.90 eV (S 2p_{1/2}) could be assigned to the S²⁻ state, as shown in Fig. 4d. The binding energies of Mn 2p, Cd 3d and S 2p agreed well with the values reported in the previous work [11,13,14]. The Co 2p XPS spectrum displayed in Fig. 4e could divided into four peaks. The peaks at 795.58 and 779.29 eV could be attribute to Co 2p_{1/2} and Co 2p_{3/2}, respectively, and the peaks at 783.28 and 800.88 eV were the satellite peaks [52–54]. As shown in Fig. 4f, the P 2p peaks located at 130.59 and 129.30 eV were in accordance with the P 2p_{1/2} and P 2p_{3/2} in the CoP₃ [52,54]. Meanwhile, the peak at 134.59 eV was assigned to oxidized P species due to the superficial oxidation of CoP₃ upon exposing to air [55,56]. All these results above further proved that Mn_{0.2}Cd_{0.8}S/CoP₃ composite was composed of Mn_{0.2}Cd_{0.8}S and CoP₃. Moreover, the comparisons between the typical binding energies of Co metal,

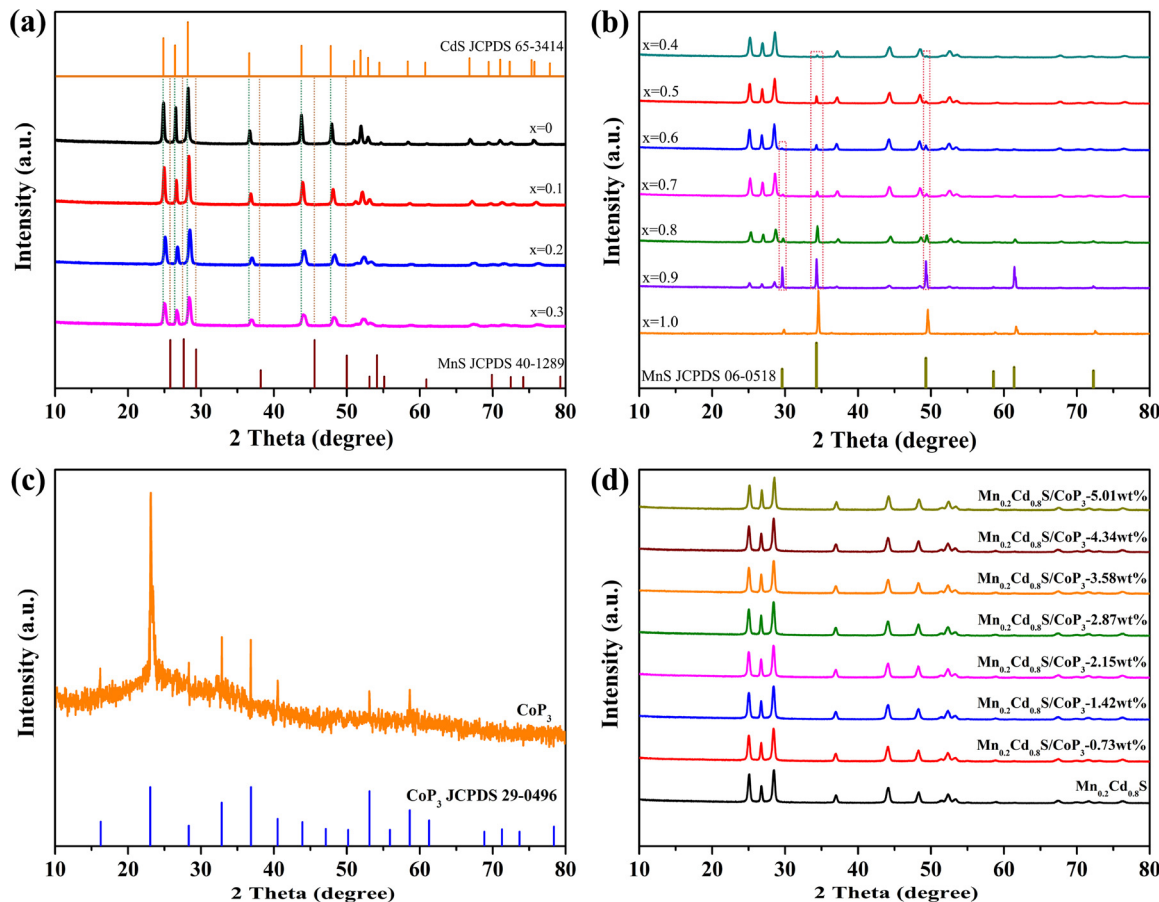


Fig. 1. XRD patterns of (a) $Mn_xCd_{1-x}S$ ($0 \leq x \leq 0.3$) together with the standard diffraction patterns of CdS and γ -MnS, (b) $Mn_xCd_{1-x}S$ ($0.4 \leq x \leq 1$) and the standard diffraction patterns of a-MnS, (c) as-prepared CoP_3 and its standard diffraction patterns, (d) $Mn_{0.2}Cd_{0.8}S/CoP_3$ composites loading with different content of CoP_3 .

elemental S and P and those of Co 2p_{3/2}, S 2p_{3/2} and P 2p_{3/2} in $Mn_{0.2}Cd_{0.8}S/CoP_3$ -2.87 wt% composite were further investigated. Compared with the typical binding energy of Co metal (778.1–778.2 eV) [57], the energy level of Co 2p_{3/2} in composite shifted to high energy, indicating the Co atom in composite has a partial positive charge (δ^+). In contrast, the binding energy of S 2p_{3/2} and P 2p_{3/2} in composite exhibited a negative shift relative to that of elemental S (163.7 eV) [57] and P (130 eV) [58], respectively, suggesting the partially negatively charged S (δ^-) and P (δ^-). These results further inferred that the $Co(\delta^+)-S(\delta^-)$ and $Co(\delta^+)-P(\delta^-)$ bonding states exist on the surface of $Mn_{0.2}Cd_{0.8}S/CoP_3$ composite due to the charge redistribution between Co to S and P atoms. These surface bonding states were not only critical for understanding the interaction between CoP_3 and $Mn_{0.2}Cd_{0.8}S$ but also beneficial for enhancing the charge transfer and improving the photocatalytic H₂ evolution activity and stability.

3.4. BET surface areas and pore size distributions

The N₂ adsorption–desorption isotherms and pore size distribution of the $Mn_{0.2}Cd_{0.8}S$ and $Mn_{0.2}Cd_{0.8}S/CoP_3$ -2.87 wt% composite were displayed in Fig. 5. $Mn_{0.2}Cd_{0.8}S$ and composite samples exhibited a typical IV isotherm with a high adsorption capacity in the P/P₀ range of 0.9–1.0 [59], implying the existence of plentiful mesopores and macropores due to the random aggregation of samples [60,61], as shown in Fig. 5a. Pore size distribution curves indicated that the two samples exhibited wide pore size distribution from 2 to 130 nm, further confirming the porous structure of samples (Fig. 5b). The $Mn_{0.2}Cd_{0.8}S/CoP_3$ -2.87 wt% composite exhibited a higher BET surface area of $46.3 \text{ m}^2 \text{ g}^{-1}$, which was higher than that of $Mn_{0.2}Cd_{0.8}S$ ($37.9 \text{ m}^2 \text{ g}^{-1}$).

The increased surface area could be attributed to the loading of CoP_3 on the surface of $Mn_{0.2}Cd_{0.8}S$, thus facilitating the increase of active sites and enhancement of photocatalytic H₂ evolution activity.

3.5. UV-vis DRS analysis

A comparison of the UV-vis DRS of CoP_3 , $Mn_{0.2}Cd_{0.8}S$ and $Mn_{0.2}Cd_{0.8}S/CoP_3$ composite was displayed in Fig. 6a. Pure CoP_3 displayed a humped absorption peak in the visible light and near-infrared region due to its narrow band gap. The absorption edge of $Mn_{0.2}Cd_{0.8}S$ was estimated to be about 515 nm. For $Mn_{0.2}Cd_{0.8}S/CoP_3$ composite, the absorption edge at 500–600 nm did not display obvious red shift when the CoP_3 loading amount changed varying from 0.73 to 2.15 wt %, which was ascribed to the low loading content of CoP_3 . With increasing the CoP_3 content from 2.87 to 5.01 wt %, the absorption edge of composite displayed an obvious red shift due to the intrinsic absorption of black-colored CoP_3 nanoparticles. More importantly, compared with the pure $Mn_{0.2}Cd_{0.8}S$, all $Mn_{0.2}Cd_{0.8}S/CoP_3$ composites appeared apparently a new absorption peak at about 700 nm, indicating the successful incorporation of CoP_3 . The intensity of the new absorption peak enhanced gradually as CoP_3 content increased, which could be ascribed to the intimate interfacial contact between $Mn_{0.2}Cd_{0.8}S$ and CoP_3 . In particular, the strongest absorption intensity was achieved by loading 2.87 wt% CoP_3 . However, the further increase of CoP_3 content resulted in the decrease of absorption intensity, attributing to the shielding effect that the excessive black CoP_3 partially blocked the light absorption of $Mn_{0.2}Cd_{0.8}S$. It is believed that the enhanced light absorption of certain $Mn_{0.2}Cd_{0.8}S/CoP_3$ composite is favorable to generate more available photogenerated electrons for participating in the

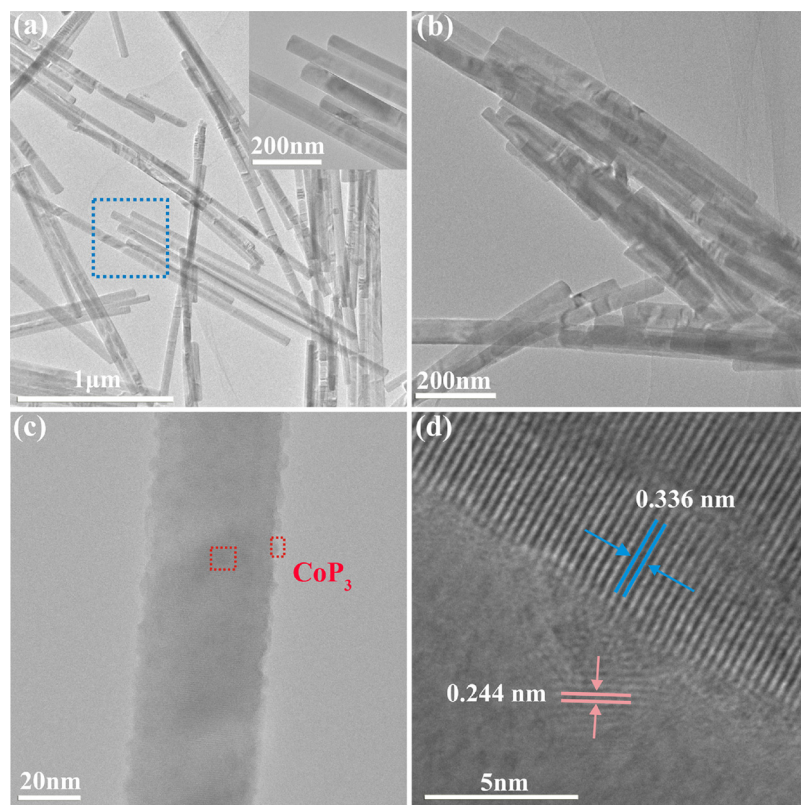


Fig. 2. TEM images of (a) $\text{Mn}_{0.2}\text{Cd}_{0.8}\text{S}$ and (b) $\text{Mn}_{0.2}\text{Cd}_{0.8}\text{S}/\text{CoP}_3$ -2.87 wt% composite, (c and d) HRTEM images of $\text{Mn}_{0.2}\text{Cd}_{0.8}\text{S}/\text{CoP}_3$ -2.87 wt% composite. (For interpretation of the references to colour in the text, the reader is referred to the web version of this article.)

photocatalytic reaction towards H_2 evolution. The corresponding energy band gaps of $\text{Mn}_{0.2}\text{Cd}_{0.8}\text{S}$ and CoP_3 could be obtained according to the Tauc plots of $(ahv)^2$ versus hv , as shown in Fig. 6b. The band gap values of $\text{Mn}_{0.2}\text{Cd}_{0.8}\text{S}$ and CoP_3 were estimated to be 2.41 and 1.70 eV, respectively. The valence band potential (E_{VB}) and conduction band potential (E_{CB}) of $\text{Mn}_{0.2}\text{Cd}_{0.8}\text{S}$ and CoP_3 could be determined by the VB-XPS spectra and the equation of $E_{\text{CB}} = E_{\text{VB}} - Eg$. As shown in Fig. S2, the E_{VB} value of $\text{Mn}_{0.2}\text{Cd}_{0.8}\text{S}$ and CoP_3 was found to be about 1.78 and 1.32 eV according to their VB-XPS spectra. Thus, the E_{CB} value of $\text{Mn}_{0.2}\text{Cd}_{0.8}\text{S}$ and CoP_3 was calculated to be -0.63 and -0.38 eV, respectively.

3.6. Photocatalytic activity and stability

The photocatalytic H_2 evolution activities of the as-prepared samples were investigated under visible light irradiation ($\lambda \geq 420$ nm) using $0.5 \text{ mol L}^{-1} \text{Na}_2\text{S}/0.5 \text{ mol L}^{-1} \text{Na}_2\text{SO}_3$ aqueous solution as a sacrificial agent. Fig. 7a showed the photocatalytic H_2 evolution performance of $\text{Mn}_x\text{Cd}_{1-x}\text{S}$ ($0 \leq x \leq 0.3$) samples. Pure CdS displayed a low photocatalytic H_2 evolution rate of $1.63 \text{ mmol g}^{-1} \text{h}^{-1}$. With increasing the value of x , the H_2 evolution activities increased dramatically and then decreased. $\text{Mn}_{0.2}\text{Cd}_{0.8}\text{S}$ showed the highest H_2 evolution rate of $5.88 \text{ mmol g}^{-1} \text{h}^{-1}$, suggesting its suitable band gap and position are best for the visible-light-driven photocatalytic H_2 evolution. Our group [14] have reported the $\text{Mn}_x\text{Cd}_{1-x}\text{S}$ ($0.05 \leq x \leq 0.45$) solid solution with irregular polyhedral morphology and confirmed that $\text{Mn}_{0.25}\text{Cd}_{0.75}\text{S}$ has the highest H_2 evolution rate under visible light irradiation ($\lambda \geq 400$ nm). For comparison, the H_2 evolution rate of $\text{Mn}_{0.25}\text{Cd}_{0.75}\text{S}$ was also evaluated under visible light irradiation ($\lambda \geq 420$ nm). The result indicated that irregular polyhedral $\text{Mn}_{0.25}\text{Cd}_{0.75}\text{S}$ sample has a low H_2 evolution rate of $0.93 \text{ mmol g}^{-1} \text{h}^{-1}$, confirming that 1D nanowires structure was conducive to promote the separation of photogenerated charge carriers and

enhance the photocatalytic H_2 evolution activity.

Fig. 7b showed the photocatalytic H_2 evolution rate of $\text{Mn}_{0.2}\text{Cd}_{0.8}\text{S}/\text{CoP}_3$ composites with different contents of CoP_3 . No H_2 was detected when CoP_3 alone was used as a photocatalyst, suggesting its very poor photocatalytic activity for H_2 evolution. $\text{Mn}_{0.2}\text{Cd}_{0.8}\text{S}$ displayed a relatively low photocatalytic activity, probably because of the high recombination of photogenerated electron-hole pairs. However, once CoP_3 was introduced onto $\text{Mn}_{0.2}\text{Cd}_{0.8}\text{S}$ NWs, the H_2 evolution activity was significantly enhanced even the loading was as low as 0.73 wt %, indicating that CoP_3 was acted very well as a co-catalyst of $\text{Mn}_{0.2}\text{Cd}_{0.8}\text{S}$. With the increase of the loading content of CoP_3 , the H_2 evolution rate of composite was further increased. In particular, the best performance was achieved at a 2.87 wt% loading of CoP_3 . The highest H_2 evolution rate reached $29.53 \text{ mmol g}^{-1} \text{h}^{-1}$, which was about 5.02 times higher than that of $\text{Mn}_{0.2}\text{Cd}_{0.8}\text{S}$ alone. The AQE of $\text{Mn}_{0.2}\text{Cd}_{0.8}\text{S}/\text{CoP}_3$ -2.87 wt% was calculated to be 29.2% at 420 nm. However, the further increase of CoP_3 loading content resulted in the decrease of H_2 evolution rate. For example, when CoP_3 loading reached to 5.01 wt%, the H_2 evolution rate dramatically decreased to $20.75 \text{ mmol g}^{-1} \text{h}^{-1}$. The reason for the decrease could be ascribed to the shielding effect that the excessive black CoP_3 will partially block the light absorption of $\text{Mn}_{0.2}\text{Cd}_{0.8}\text{S}$. Besides, the active sites for H_2 evolution could be covered by excessive CoP_3 , thus hindering the effective contact between the active sites and the reactants. Therefore, loading appropriate amounts of CoP_3 co-catalyst can optimize the photocatalytic activity of the $\text{Mn}_{0.2}\text{Cd}_{0.8}\text{S}$ solid solution. To further understand the promoting role of loading CoP_3 in enhancing the H_2 evolution rate of $\text{Mn}_{0.2}\text{Cd}_{0.8}\text{S}$, some selected cobalt phosphide-based heterostructured photocatalyst systems for H_2 evolution were summarized in Table S3. As shown in Table S3, the H_2 evolution rate of $\text{Mn}_{0.2}\text{Cd}_{0.8}\text{S}/\text{CoP}_3$ -2.87 wt% composite appeared to be higher than those of most of the reported photocatalysts, which were tested in a wide range of conditions in the literature although light source, light intensity, sacrificial reagent and so on should be the same

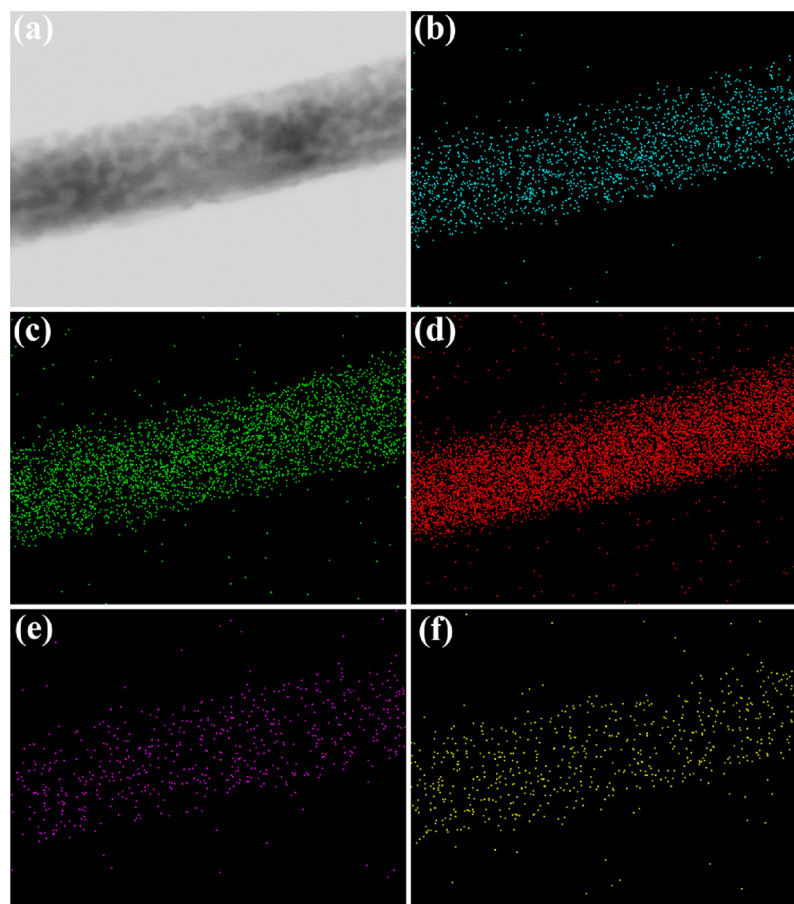


Fig. 3. STEM-EDX image of (a) Mn_{0.2}Cd_{0.8}S/CoP₃-2.87 wt% composite and the corresponding element mapping for (b) Mn, (c) Cd, (d) S, (e) Co and (f) P.

for a fairer comparison. These comparisons further indicated that CoP₃ is important to enhance the photocatalytic activity of Mn_{0.2}Cd_{0.8}S solid solution due to its positive effect for H₂ evolution.

For comparison, we have prepared the sample of Mn_{0.2}Cd_{0.8}S/Pt-1.5 wt% as reference photocatalyst by the typical photodeposition method using H₂PtCl₆ as the precursor. The photocatalytic activity test in Fig. 7c indicated that loading Pt can significantly enhance the H₂ evolution activity of Mn_{0.2}Cd_{0.8}S. The H₂ evolution amount over Mn_{0.2}Cd_{0.8}S/Pt-1.5 wt% reached 65.86 mmol g⁻¹, which is 2.8 times higher than that of Mn_{0.2}Cd_{0.8}S (23.52 mmol g⁻¹). However, the value was still much lower than that of Mn_{0.2}Cd_{0.8}S/CoP₃-2.87 wt% (118.13 mmol g⁻¹), indicating that CoP₃ is a highly efficient co-catalyst for enhancing the activity of Mn_{0.2}Cd_{0.8}S toward H₂ evolution. Furthermore, it was also demonstrated that the H₂ evolution amount (24.65 mmol g⁻¹) of the mechanical mixture of Mn_{0.2}Cd_{0.8}S and CoP₃ (2.87 wt%) was much weaker than that of Mn_{0.2}Cd_{0.8}S/CoP₃-2.87 wt% composite, further confirming the important functions of the heterojunction between CoP₃ and Mn_{0.2}Cd_{0.8}S in enhancing the H₂ evolution activity.

To confirm the photocatalytic stability of Mn_{0.2}Cd_{0.8}S/CoP₃ composite, we performed six consecutive H₂ evolution runs over Mn_{0.2}Cd_{0.8}S/CoP₃-2.87 wt% sample under the same conditions. Each cycle was performed for 4 h under visible light irradiation ($\lambda \geq 420$ nm) and the result was displayed in Fig. 7d. After six recycles, a total of 107.11 mmol g⁻¹ H₂ was produced, which was almost 9.33% of H₂ production activity loss, suggesting its good stability. This fact can be further supported by the XRD patterns of Mn_{0.2}Cd_{0.8}S/CoP₃-2.87 wt% composite before and after photocatalytic H₂ evolution reaction (Fig. S3), which revealed that composite after six cyclic runs still exhibited the phase structure similar to those of the as-prepared fresh composite.

3.7. Charge transfer and separation

The PL and TRPL spectra have been applied to explore the transfer and separation efficiency of photogenerated charge. Fig. 8a showed PL spectra of Mn_{0.2}Cd_{0.8}S and Mn_{0.2}Cd_{0.8}S/CoP₃-2.87 wt% composite with their emission peaks both centered at 539 nm. As a contrast, the intensity of PL emission peak for Mn_{0.2}Cd_{0.8}S/CoP₃ composite was much weaker than that of Mn_{0.2}Cd_{0.8}S, attributing to the rapid charge transfer from Mn_{0.2}Cd_{0.8}S to CoP₃, which benefits to suppress the electron-hole recombination and enhance the photocatalytic activity. The TRPL spectra shown in Fig. 8b further indicated that the charge carriers lifetime of Mn_{0.2}Cd_{0.8}S/CoP₃-2.87 wt% composite (0.8697 ns) was higher than that of pure Mn_{0.2}Cd_{0.8}S (0.5256 ns). It was obvious that the charge carriers lifetime of Mn_{0.2}Cd_{0.8}S was prolonged upon loading CoP₃, facilitating more photogenerated electrons participating in the photocatalytic reaction towards H₂ evolution.

The separation efficiency of photogenerated carriers can be further investigated by the photocurrent and EIS measurements. Fig. 9a displayed the periodic on/off photocurrent response of the Mn_{0.2}Cd_{0.8}S and Mn_{0.2}Cd_{0.8}S/CoP₃-2.87 wt% composite. As shown in Fig. 9a, it was obviously that the photocurrent density for Mn_{0.2}Cd_{0.8}S/CoP₃ composite was much higher than that of Mn_{0.2}Cd_{0.8}S, suggesting a distinct improvement in the suppression of photogenerated electron-hole recombination, which was well consistent with the results of PL spectra shown in Fig. 8a. Furthermore, EIS Nyquist plots was also performed to explore the advantage of Mn_{0.2}Cd_{0.8}S/CoP₃ composite over Mn_{0.2}Cd_{0.8}S in the transport processes of photogenerated electron-hole pairs. As displayed in Fig. 9b, a smaller arcs has been observed for Mn_{0.2}Cd_{0.8}S/CoP₃ composite as compared to that of Mn_{0.2}Cd_{0.8}S, further indicating lower charge transfer resistance and thus a higher transfer rate of electron-hole pairs in the Mn_{0.2}Cd_{0.8}S/CoP₃ composite.

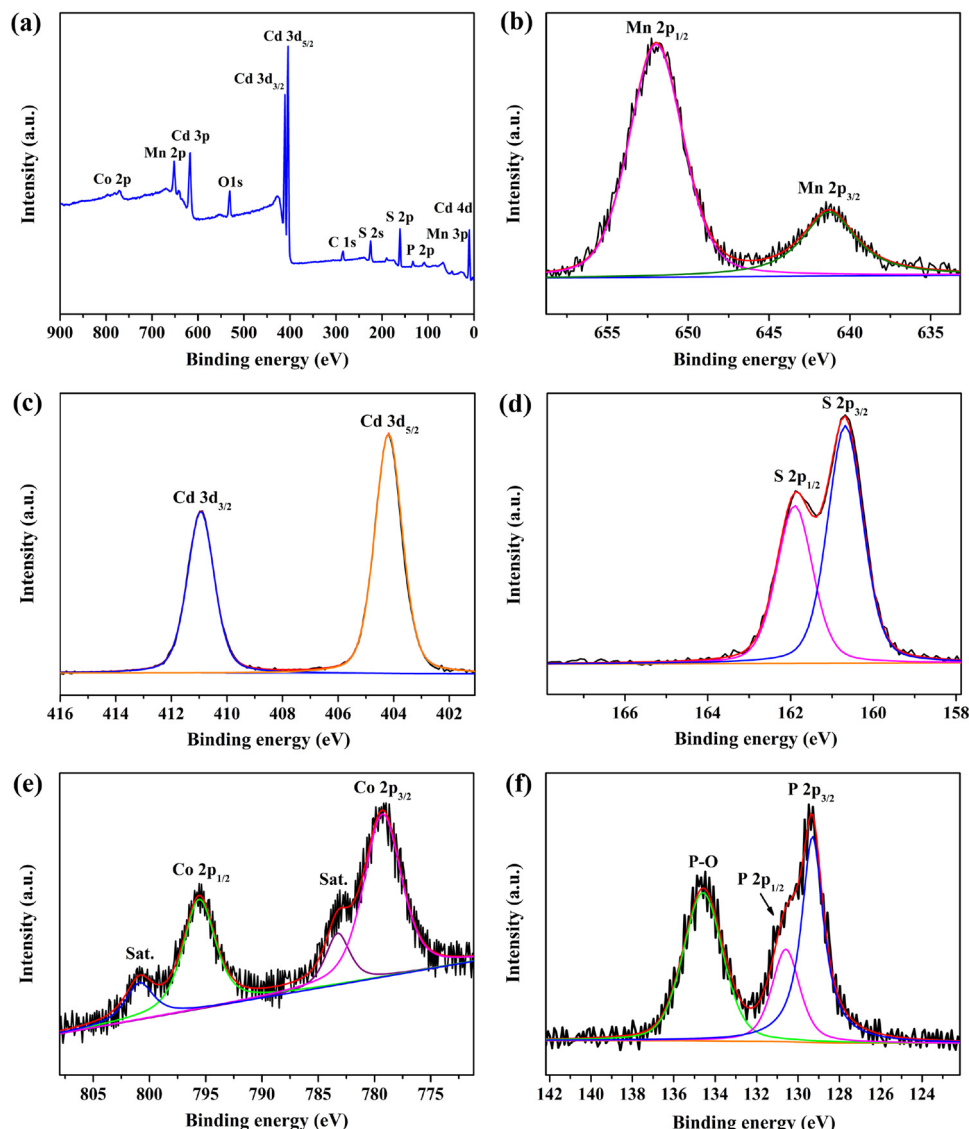


Fig. 4. The XPS spectra of $\text{Mn}_{0.2}\text{Cd}_{0.8}\text{S}/\text{CoP}_3$ -2.87 wt% composite: (a) survey, (b) Mn 2p, (c) Cd 3d, (d) S 2p, (e) Co 2p and (f) P 2p.

3.8. Photocatalytic mechanism

Based on all the above results, a proposed mechanism for the photocatalytic H_2 evolution of $\text{Mn}_{0.2}\text{Cd}_{0.8}\text{S}/\text{CoP}_3$ photocatalyst was illustrated in Fig. 10. Loading CoP_3 on the surface of $\text{Mn}_{0.2}\text{Cd}_{0.8}\text{S}$ NWs can obtain the superior interfacial contacts between $\text{Mn}_{0.2}\text{Cd}_{0.8}\text{S}$ and CoP_3 , which provides a feasible route to promote interfacial charge transfer and inhibit the recombination of photogenerated electron-hole pairs. Under visible-light irradiation, $\text{Mn}_{0.2}\text{Cd}_{0.8}\text{S}$ NWs could be easily

activated and generated electron-hole pairs. Since $\text{Mn}_{0.2}\text{Cd}_{0.8}\text{S}$ possessed more negative CB level (-0.63 eV) as compared with the CB potential (-0.38 eV) of CoP_3 , the ample thermodynamic driving force efficiently accelerated the electrons transfer from the CB of $\text{Mn}_{0.2}\text{Cd}_{0.8}\text{S}$ to that of CoP_3 . And thus, the accumulated electrons in the CoP_3 directly reduced H^+ ions to produce H_2 . Meanwhile, the holes that remained on the surface of the $\text{Mn}_{0.2}\text{Cd}_{0.8}\text{S}$ were consumed by the sacrificial reagents, further boosting charge separation. In addition, CoP_3 not only acted as electron collector to capture the photogenerated

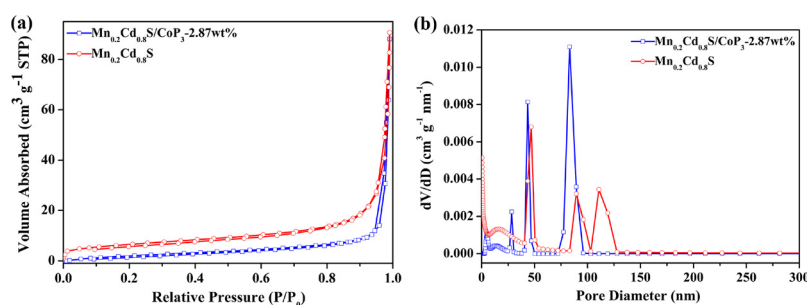


Fig. 5. (a) Nitrogen adsorption–desorption isotherms and (b) corresponding pore size distributions of $\text{Mn}_{0.2}\text{Cd}_{0.8}\text{S}$ and $\text{Mn}_{0.2}\text{Cd}_{0.8}\text{S}/\text{CoP}_3$ -2.87 wt% composite.

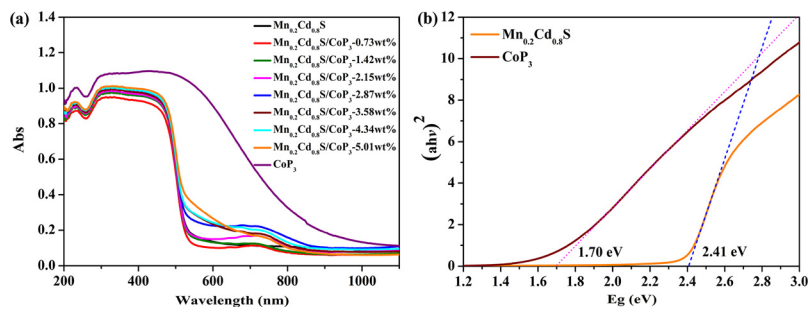


Fig. 6. (a) UV-vis DRS spectra of CoP₃, Mn_{0.2}Cd_{0.8}S and Mn_{0.2}Cd_{0.8}S/CoP₃ composites, (b) band gap of CoP₃ and Mn_{0.2}Cd_{0.8}S.

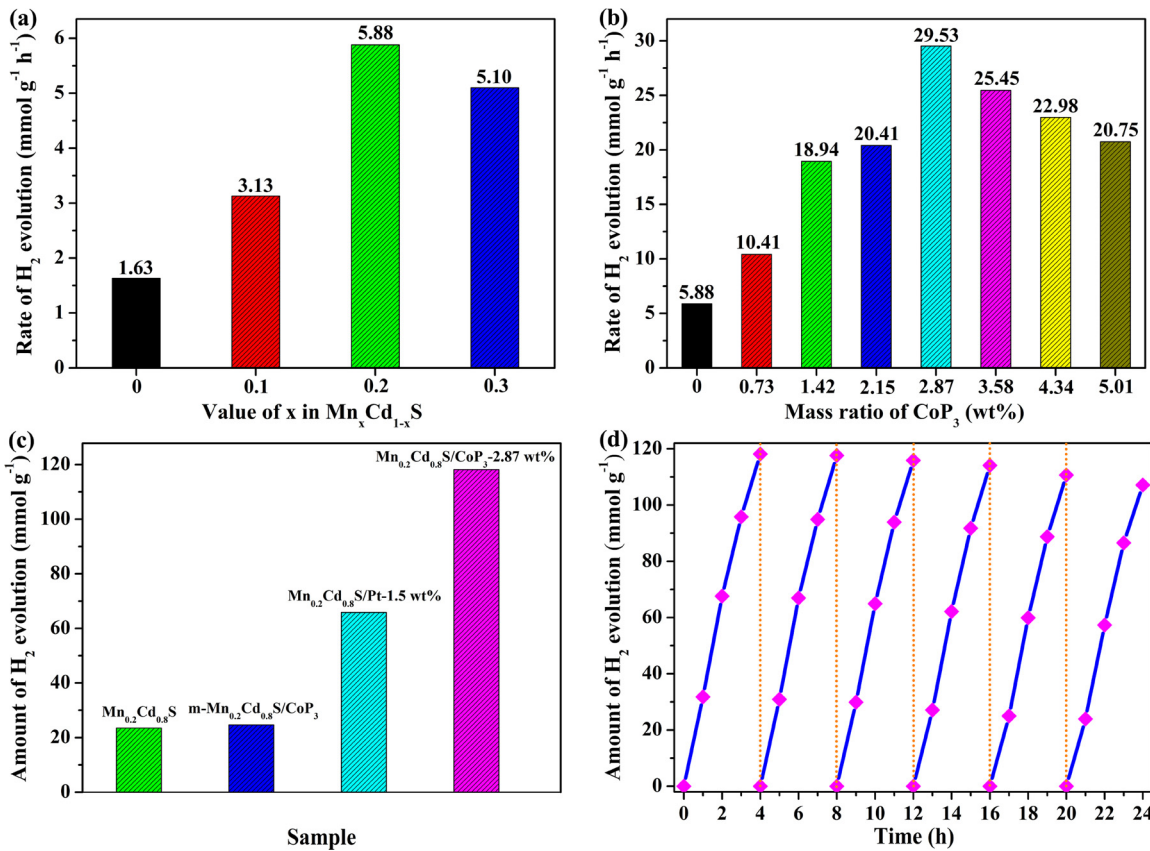


Fig. 7. H₂ evolution rate of (a) Mn_xCd_{1-x}S ($0 \leq x \leq 0.3$) and (b) Mn_{0.2}Cd_{0.8}S/CoP₃ composites with different CoP₃ content for 4 h, (c) comparison of H₂ evolution amount of Mn_{0.2}Cd_{0.8}S/CoP₃-2.87 wt% composite with Mn_{0.2}Cd_{0.8}S, Mn_{0.2}Cd_{0.8}S/Pt-1.5 wt% and m-Mn_{0.2}Cd_{0.8}S/CoP₃ (simple mechanical mixture of Mn_{0.2}Cd_{0.8}S and 2.87 wt% CoP₃) for 4 h, (d) cycling test of photocatalytic H₂ evolution over Mn_{0.2}Cd_{0.8}S/CoP₃-2.87 wt% composite.

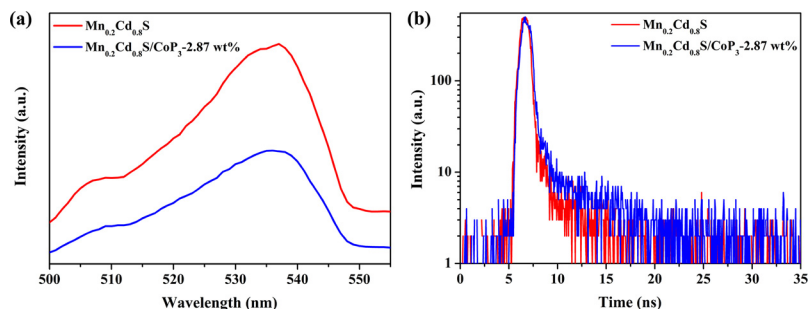


Fig. 8. (a) PL spectra of Mn_{0.2}Cd_{0.8}S and Mn_{0.2}Cd_{0.8}S/CoP₃-2.87 wt% composite ($\lambda_{\text{exc}} = 331$ nm), (b) TRPL spectra for Mn_{0.2}Cd_{0.8}S and Mn_{0.2}Cd_{0.8}S/CoP₃-2.87 wt% composite detected at 539 nm (the excitation source is a 377.8 nm laser).

electrons and prolong the lifetime of the charge carriers, but also served as an effective active site to accelerate the H₂ evolution reaction [52], thus enhancing the photocatalytic H₂ evolution activity of Mn_{0.2}Cd_{0.8}S.

Consequently, we proposed two main factors to explain why the Mn_{0.2}Cd_{0.8}S/CoP₃ composite could achieve the outstanding photocatalytic activity towards H₂ evolution: (1) The heterojunctions

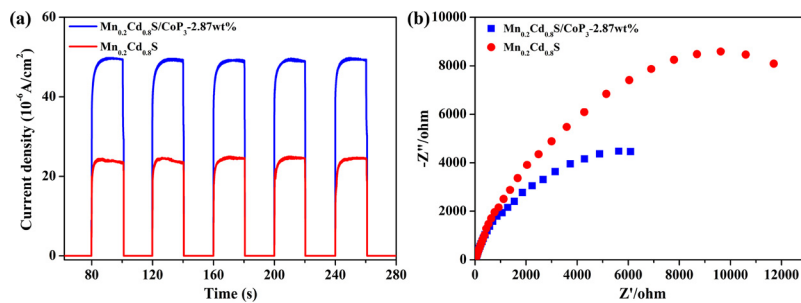


Fig. 9. (a) I-t curves and (b) EIS Nyquist plots of $\text{Mn}_{0.2}\text{Cd}_{0.8}\text{S}$ and $\text{Mn}_{0.2}\text{Cd}_{0.8}\text{S}/\text{CoP}_3$ -2.87 wt% composite.

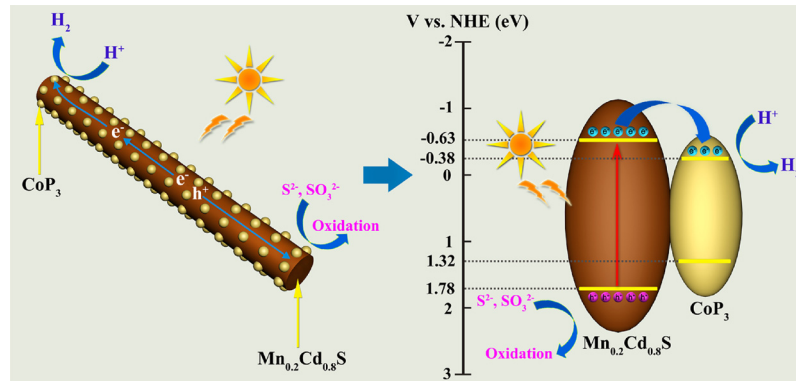


Fig. 10. Schematic illustration for the charge transfer and separation in $\text{Mn}_{0.2}\text{Cd}_{0.8}\text{S}/\text{CoP}_3$ system and proposed mechanism for enhanced photocatalytic H_2 evolution under visible light irradiation.

constructed by loading CoP_3 co-catalyst on the surface of $\text{Mn}_{0.2}\text{Cd}_{0.8}\text{S}$ NWs greatly promoted the separation of photogenerated charge carriers. (2) CoP provided abundant active sites for H_2 evolution reaction.

4. Conclusions

In conclusion, with the combination of morphological control and co-catalyst modification, a highly efficient $\text{Mn}_{0.2}\text{Cd}_{0.8}\text{S}/\text{CoP}_3$ composite was rationally designed and synthesized by a facile solvothermal method. CoP_3 tightly loading on the surface of $\text{Mn}_{0.2}\text{Cd}_{0.8}\text{S}$ NWs formed the intimate contact interfaces, facilitating the charge separation and providing more active sites for H_2 evolution reaction. As a result, the $\text{Mn}_{0.2}\text{Cd}_{0.8}\text{S}/\text{CoP}_3$ composite exhibited an outstanding photocatalytic H_2 evolution activity. The highest H_2 evolution rate of $29.53 \text{ mmol g}^{-1} \text{ h}^{-1}$ (with an AQE of 29.2% at 420 nm) was obtained over $\text{Mn}_{0.2}\text{Cd}_{0.8}\text{S}/\text{CoP}_3$ -2.87 wt% composite, which was 5.02 times than that of pure $\text{Mn}_{0.2}\text{Cd}_{0.8}\text{S}$ NWs and 1.79 times than that of the optimized $\text{Mn}_{0.2}\text{Cd}_{0.8}\text{S}/\text{Pt}$ sample. In addition, the $\text{Mn}_{0.2}\text{Cd}_{0.8}\text{S}/\text{CoP}_3$ composite exhibited a good stability. The results illustrated that CoP_3 was an efficient and robust noble-metal-free co-catalyst for $\text{Mn}_{0.2}\text{Cd}_{0.8}\text{S}$, which may be also potentially used in photocatalytic H_2 evolution for other photocatalysts. It is expected that the present work can provide basic principles for the development of noble-metal-free co-catalysts with high photocatalytic activity and general applicability.

Acknowledgements

We gratefully acknowledge the support of this research by the National Natural Science Foundation of China (Nos. 21671176, 21471133 and 21541011), Foundation of He'nan Educational Committee, China (No. 14A150001), and Key Science and Technology Program of Zhengzhou, China (No: 141PQYJS562).

Appendix A. Supplementary data

Supplementary data associated with this article can be found, in the online version, at <https://doi.org/10.1016/j.apcatb.2018.06.040>.

References

- [1] X. Feng, S. Maier, M. Salmeron, J. Am. Chem. Soc. 134 (2012) 5662–5668.
- [2] K.C. Christoforidis, P. Fornasiero, ChemCatChem 9 (2017) 1523–1544.
- [3] M.R. Hoffmann, S.T. Martin, W. Choi, D.W. Bahnemann, Chem. Rev. 95 (1995) 69–96.
- [4] A. Kudo, Y. Misaki, Chem. Soc. Rev. 38 (2009) 253–278.
- [5] A. Fujishima, K. Honda, Nature 238 (1972) 37–38.
- [6] K. Ikeue, S. Shiba, M. Machida, Chem. Mater. 22 (2010) 743–745.
- [7] M.Y. Liu, L.Q. Zhang, X.X. He, B. Zhang, H.F. Song, S.N. Li, W.S. You, J. Mater. Chem. A 2 (2014) 4619–4626.
- [8] H. Liu, J.C. Meng, J. Zhang, Catal. Sci. Technol. 7 (2017) 3802–3811.
- [9] K. Ikeue, S. Shiba, M. Machida, ChemSusChem 4 (2011) 269–273.
- [10] K. Ikeue, Y. Shimura, M. Machida, Appl. Catal. B 123–124 (2012) 84–88.
- [11] H. Liu, Z.Z. Xu, Z. Zhang, D. Ao, Appl. Catal. A 518 (2016) 150–157.
- [12] Q.Z. Huang, J.C. Wang, L.Q. Ye, Q. Zhang, H.C. Yao, Z.J. Li, J. Taiwan Inst. Chem. Eng. 80 (2017) 570–577.
- [13] X.L. Liu, X.Z. Liang, P. Wang, B.B. Huang, X.Y. Qin, X.Y. Zhang, Y. Dai, Appl. Catal. B 203 (2017) 282–288.
- [14] Q.Z. Huang, Y. Xiong, Q. Zhang, H.C. Yao, Z.J. Li, Appl. Catal. B 209 (2017) 514–522.
- [15] H.S. Zhai, X.L. Liu, P. Wang, B.B. Huang, Q.Q. Zhang, Appl. Surf. Sci. 430 (2018) 515–522.
- [16] X.L. Liu, Q. Liu, P. Wang, Y.Z. Liu, B.B. Huang, E.A. Rozhkova, Q.Q. Zhang, Z.Y. Wang, Y. Dai, J. Lu, Chem. Eng. J. 337 (2018) 480–487.
- [17] S. Liu, Z.R. Tang, Y. Sun, J.C. Colmenares, Y.J. Xu, Chem. Soc. Rev. 44 (2015) 5053–5075.
- [18] B. Weng, S. Liu, Z.R. Tang, Y.J. Xu, RSC Adv. 4 (2014) 12685–12700.
- [19] K.R. Yoon, J.W. Ko, D.Y. Youn, C.B. Park, I.D. Kim, Green Chem. 18 (2016) 944–950.
- [20] Z.R. Tang, B. Han, C. Han, Y.J. Xu, J. Mater. Chem. A 5 (2017) 2387–2410.
- [21] J.R. Ran, J. Zhang, J.G. Yu, M. Jaroniec, S.Z. Qiao, Chem. Soc. Rev. 43 (2014) 7787–7812.
- [22] J.H. Yang, D.G. Wang, H.X. Han, C. Li, Acc. Chem. Res. 46 (2013) 1900–1909.
- [23] S. Bai, W.J. Yin, L.L. Wang, Z.Q. Li, Y.J. Xiong, RSC Adv. 6 (2016) 57446–57463.
- [24] Z.J. Sun, H.F. Zheng, J.S. Li, P.W. Du, Energy Environ. Sci. 8 (2015) 2668–2676.
- [25] W.L. Zhen, X.F. Ning, B.J. Yang, Y.Q. Wu, Z. Li, G.X. Lu, Appl. Catal. B 221 (2018) 243–257.
- [26] D.Q. Zeng, W.J. Xu, W.J. Ong, J. Xu, H. Ren, Y.Z. Chen, H.F. Zheng, D.L. Peng, Appl.

- Catal. B 221 (2018) 47–55.
- [27] Z.W. Pan, R. Wang, J.N. Li, S. Iqbal, W. Liu, K.B. Zhou, Int. J. Hydrogen Energy 43 (2018) 5337–5345.
- [28] Z.J. Sun, H.B. Chen, Q. Huang, P.W. Du, Catal. Sci. Technol. 5 (2015) 4964–4967.
- [29] S.M. Yin, J.Y. Han, Y.J. Zou, T.H. Zhou, R. Xu, Nanoscale 8 (2016) 14438–14447.
- [30] Q.D. Yue, Y.Y. Wan, Z.J. Sun, X.J. Wu, Y.P. Yuan, P.W. Du, J. Mater. Chem. A 3 (2015) 16941–16947.
- [31] X. Liu, X.Q. Li, L.X. Qin, J. Mu, S.Z. Kang, J. Mater. Chem. A 5 (2017) 14682–14688.
- [32] J.X. Zhang, W.F. Yao, C.P. Huang, P.H. Shi, Q.J. Xu, J. Mater. Chem. A 5 (2017) 12513–12519.
- [33] S. Cao, Y. Chen, C.C. Hou, X.J. Lv, W.F. Fu, J. Mater. Chem. A 3 (2015) 6096–6101.
- [34] J.M. Wang, Z. Liu, Y.W. Zheng, L. Cui, W.R. Yang, J.Q. Liu, J. Mater. Chem. A 5 (2017) 22913–22932.
- [35] S. Cao, Y. Chen, C.J. Wang, X.J. Lv, W.F. Fu, Chem. Commun. 51 (2015) 8708–8711.
- [36] Z.J. Sun, B.H. Lv, J.S. Li, M. Xiao, X.Y. Wang, P.W. Du, J. Mater. Chem. A 4 (2016) 1598–1602.
- [37] W.T. Bi, L. Zhang, Z.T. Sun, X.G. Li, T. Jin, X.J. Wu, Q. Zhang, Y. Luo, C.Z. Wu, Y. Xie, ACS Catal. 6 (2016) 4253–4257.
- [38] D.A. Reddy, J. Choi, S. Lee, Y. Kim, S. Hong, D.P. Kumar, T.K. Kim, Catal. Sci. Technol. 6 (2016) 6197–6206.
- [39] Y.M. Dong, L.G. Kong, G.L. Wang, P.P. Jiang, N. Zhao, H.Z. Zhang, Appl. Catal. B 211 (2017) 245–251.
- [40] D. Zhao, B. Sun, X.Q. Li, L.X. Qin, S.Z. Kang, D. Wang, RSC Adv. 6 (2016) 33120–33125.
- [41] X.Z. Yue, S.S. Yi, R.W. Wang, Z.T. Zhang, S.L. Qiu, Small 13 (2017) 1603301.
- [42] S.S. Yi, J.M. Yan, B.R. Wulan, S.J. Li, K.H. Liu, Q. Jiang, Appl. Catal. B 200 (2017) 477–483.
- [43] W. Liu, L.L. Cao, W.R. Cheng, Y.J. Cao, X.K. Liu, W. Zhang, X.L. Mou, L.L. Jin, X.S. Zheng, W. Che, Q.H. Liu, T. Yao, S.Q. Wei, Angew. Chem. Int. Ed. 56 (2017) 9312–9317.
- [44] B.C. Qiu, Q.H. Zhu, M.Y. Xing, J.L. Zhang, Chem. Commun. 53 (2017) 897–900.
- [45] D.S. Dai, H. Xu, L. Ge, C.C. Han, Y.Q. Gao, S.S. Li, Y. Lu, Appl. Catal. B 217 (2017) 429–436.
- [46] X.L. Yin, G.Y. He, B. Sun, W.J. Jiang, D.J. Xue, A.D. Xia, L.J. Wan, J.S. Hu, Nano Energy 28 (2016) 319–329.
- [47] L. Vegard, H. Schjelderup, Phys. Z. 18 (1917) 93–96.
- [48] J.K. Furdyna, J. Appl. Phys. 64 (1988) 3663–3664.
- [49] I. Tsuji, H. Kato, H. Kobayashi, A. Kudo, J. Am. Chem. Soc. 126 (2004) 13406–13413.
- [50] C.H. An, K.B. Tang, X.M. Liu, F.Q. Li, G.E. Zhou, Y.T. Qian, J. Cryst. Growth 252 (2003) 575–580.
- [51] D.B. Fan, X.D. Yang, H. Wang, Y.C. Zhang, H. Yan, Phys. B 337 (2003) 165–169.
- [52] T.L. Wu, M.Y. Pi, X.D. Wang, W.M. Guo, D.K. Zhang, S.J. Chen, Appl. Surf. Sci. 427 (2018) 800–806.
- [53] A.P. Grosvenor, S.D. Wik, R.G. Cavell, Inorg. Chem. 44 (2005) 8988–8998.
- [54] T.L. Wu, M.Y. Pi, X.D. Wang, D.K. Zhang, S.J. Chen, Phys. Chem. Chem. Phys. 19 (2017) 2104–2110.
- [55] J. Tian, Q. Liu, A.M. Asiri, X. Sun, J. Am. Chem. Soc. 136 (2014) 7587–7590.
- [56] Q. Liu, J. Tian, W. Cui, P. Jiang, N. Cheng, A.M. Asiri, X. Sun, Angew. Chem. 126 (2014) 6828–6832.
- [57] J.Y. Li, X.M. Zhou, Z.M. Xia, Z.Y. Zhang, J. Li, Y.Y. Ma, Y.Q. Qu, J. Mater. Chem. A 3 (2015) 13066–13071.
- [58] P. Jiang, Q. Liu, C.J. Ge, W. Cui, Z.H. Pu, A.M. Asiri, X.P. Sun, J. Mater. Chem. A 2 (2014) 14634–14640.
- [59] K.S.W. Sing, D.H. Everett, R.A.W. Haul, L. Moscou, R.A. Pierotti, J. Rouquerol, T. Siemieniewska, Pure Appl. Chem. 57 (1985) 603–619.
- [60] J.L. Yuan, J.Q. Wen, Q.Z. Gao, S.C. Chen, J.M. Li, X. Li, Y.P. Fang, Dalton Trans. 44 (2015) 1680–1689.
- [61] T.M. Di, B.C. Zhu, J. Zhang, B. Cheng, J.G. Yu, Appl. Surf. Sci. 389 (2016) 775–782.